Design and Experimental Implementation of a Quasi-Direct-Drive Leg for Optimized Jumping

Yanran Ding and Hae-Won Park

Abstract— This paper introduces a novel method for actuator design that exploits electromagnetic motors' torque and speed potential in jumping applications. We proposed a nonlinear optimization process that integrates (a) the control design to obtain the optimal ground reaction force, and (b) the mechanical design to narrow down the choices of motor/gearbox pair. Based on this method, actuators were designed and assembled into a leg prototype with two actuated degrees of freedom. Experiments demonstrated that the leg could achieve a maximum vertical jumping height of 0.62 m (2.4 times of leg length) and maximum forward jumping distance of 0.72 m (2.7 times of leg length).

I. INTRODUCTION

Small and athletic mammals can perform highly dynamic maneuvers as demonstrated by a squirrel's jumping motion in Fig. 1. Inspired by this agile biological system, we investigated the dynamic motion generation scheme of small scale robots, specifically their jumping capabilities. It is observed in nature that animals with extremely different scales can achieve the same magnitude of jumping height, given that they are geometrically similar [1]. However, smaller animals need to accelerate much faster and produce higher angular speed to reach the same take-off velocity, which provides a similar maximal reachable height [2]. This observation motivated our interest in how scaling a robotic system would change the requirements on actuator characteristics. An analogy was drawn to legged robot design in the sense that an isometrically scaled down robot requires higher actuator speed to produce comparable dynamic motion [3]. If the linkage dimension is scaled down by $\frac{1}{L}$ ($L > 1$), the required motor speed is scaled by L to produce the same end-effector velocity. On the other hand, high torque density (torque per unit mass) is desirable for dynamic robotic systems [4], because actuators need to produce forces 2.6 to 3 times of body weight for high speed locomotion [5][6]. Heavily geared motors have high torque density at the cost of increased reflected inertia and friction [7], which compromises mechanical robustness because it is prone to being damaged upon impact. Series elastic actuators (SEA) could produce variable mechanical impedance and recycle energy for high efficiency gaits. However, their force control bandwidth is limited, which would be problematic in high-speed and dynamic locomotion [8]. Direct-drive robots [9] do not use a speed reduction system, thus eliminating the problems (backlash, friction, high reflected inertia) associated with gearboxes and possessing the benefits of high transparency

Yanran Ding and Hae-Won Park are with the department of Mechanical Science and Engineering Department, University of Illinois at Urbana-Champaign, IL, 61801, USA. {yding35, haewon}@illinois.edu
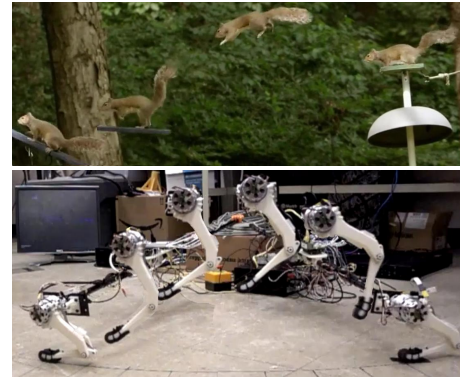
Fig. 1.   A squirrel leaping forward (top) Image courtesy of National Geographic [14]. The robot leg leaping forward (bottom)

[10] and mechanical robustness. Nevertheless, low torque density, high motor weight, and Joule heating are the main disadvantages of direct-drive. Recently, a new actuator design strategy utilizing a high-torque density electromagnetic actuator and low-gear-ratio gearbox has been introduced by a few researchers [4] (proprioceptive actuator design) [11] (quasi-direct-drive actuator). This design successfully balances between requirements for transparent transmission and high torque generation, providing an actuator design for dynamic robots that achieved diverse dynamic motions including jumping over obstacles [12] and high-speed running [13].

Inspired by this new electromagnetic actuator design strategy, this paper proposes a sequential nonlinear optimization process that solves for optimal control input and chooses mechanical design parameters simultaneously to satisfy performance requirements for a given task. As major decision variables in mechanical design, *motor sizing* and *gear ratio* were chosen to balance the requirements of the task in three aspects, namely, *torque density*, *motor speed* and *impact mitigation*. Section II introduces the dynamic models for optimization; in Section III, a nonlinear optimization problem was proposed to simultaneously select design parameters for control and mechanical design; Section IV experimentally demonstrates the jumping capability of the leg, and Section V provides the concluding remarks.

II. DYNAMIC ANALYSIS BASED ON KNEE EXTENSOR MODEL

A sequential design process was adopted to incorporate system complexity as shown in Fig. 2. The 1-DOF template [15] called knee extensor model was used to obtain the
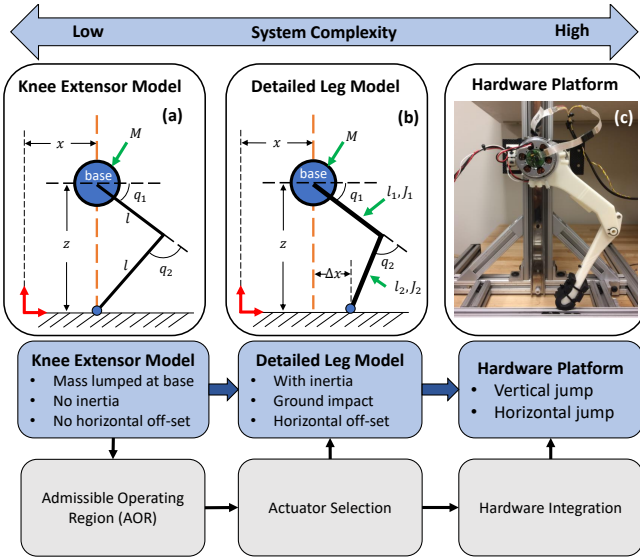
Fig. 2. Sequential design process for determining design parameters. (a) knee extensor model for motor selection (b) detailed leg model for gear ratio choice (c) hardware platform for experiments

torque and speed requirements of the desired motion from multiple optimizations, as depicted in Fig. 2(a). The motor was then chosen to meet the requirements obtained from the optimizations. A more detailed leg model with rotary inertias and horizontal foot off-set was introduced to take more design parameters into consideration, shown in Fig. 2 (b). The detailed leg model was used to determine the final choice of gear ratio by minimizing ground impact force while maintaining balance between torque and speed requirements. Optimized parameters were tested on the hardware platform shown in Fig. 2 (c) to validate the design.

A. Knee Extensor Model

A knee extensor model was used as a simple model to estimate the torque and speed requirements to perform jumping motion. Fig. 2 (a) shows the schematics of the knee extensor model, which assumes that all mass is lumped at the base, which is mounted on a vertical linear rail. Thigh and shank links have an identical length of l, while its foot and base are vertically aligned. Hence only the knee joint is actuated to perform a vertical jump while the hip joint is passive.

The dynamics of this model was formalized as a single point mass accelerated due to the ground reaction force (GRF). The ground reaction force was chosen as the control input because it is the only external force that could change the mechanical energy of the system. The equation of motion (EOM) is $\ddot{z} = \frac{F_z}{m} - g$, where z is the vertical displacement of the base, F_z is the vertical component of GRF, m is the lumped mass at the base, and g is the gravitational acceleration. A 5th order Bézier polynomial was used to parameterize GRF profile, and its coefficients are $\boldsymbol{\alpha}_F := [0, \alpha_{F1}, \alpha_{F2}, \alpha_{F3}, \alpha_{F4}, 0]^T$. The first and last coefficients were set as 0 to ensure a smooth and physically feasible ground reaction force profile.

Since a Bézier polynomial is the linear combination of a Bernstein polynomial basis [16] defined as

$$C_M(s) = \sum_{i=0}^{M} \alpha_i B_{i,M}(s) \tag{1}$$

where M is the order of Bézier polynomial, α_i is the coefficient for the ith Bernstein polynomial $B_{i,M}$, the analytical solution for velocity and position could be obtained using the property of the Bernstein polynomial [17]

$$\frac{d}{ds} B_{i,M}(s) = \frac{M}{T}(B_{i-1,M-1}(s) - B_{i,M-1}(s)) \tag{2}$$

where s is the normalized time within the time interval $[0, T]$.

Given the initial velocity $\dot{z}_0$, the velocity trajectory of stance phase could be integrated analytically using (2), providing a 6th order Bézier polynomial with coefficients $\boldsymbol{\alpha}_{\dot{z}} \in \mathbb{R}^{M+2}$. The linear relationship for integrating force Bézier coefficient to get velocity Bézier coefficient is

$$\frac{M+1}{T_{st}} \boldsymbol{\Phi}(M, T_{st}) \boldsymbol{\alpha}_{\dot{z}} = [\frac{1}{m} \boldsymbol{\alpha}_F^T - g, \dot{z}_0]^T \tag{3}$$

where T_{st} is the duration of stance, and $\boldsymbol{\Phi} \in \mathbb{R}^{(M+2) \times (M+2)}$ is a matrix whose elements are defined as

$$\boldsymbol{\Phi}_{i,j} := \begin{cases} -1, & j = i = 1, 2, \cdots, M+1 \\ 1, & j = i+1 = 2, 3, \cdots, M+2 \\ \frac{T_{st}}{M+1}, & i = M+2, j = 1 \\ 0, & \text{otherwise} \end{cases} \tag{4}$$

Similarly, the position trajectory in stance phase could also be retrieved given initial position z_0.

B. Nonlinear Optimization for Ground Reaction Force

In order to get the optimal ground reaction force profile within limits of actuator torque and velocity, an optimal control problem was formulated and solved using nonlinear optimization. Continuous time trajectories of $\boldsymbol{F}_{GRF}(t)$, $z(t)$ and $\dot{z}(t)$ were sampled at N grid points to make the optimization a finite dimensional problem. Joint angle and angular velocity at N grid points were introduced as additional optimization variables. The vector of optimization variables $\boldsymbol{x}_{opt}$ is defined as:

$$\boldsymbol{x}_{opt} := [z_0, \boldsymbol{\alpha}_{F(1-4)}^T, T_{st}, vec(\boldsymbol{q})^T, vec(\dot{\boldsymbol{q}})^T]^T \tag{5}$$

where z_0 is the base's vertical initial position, $\boldsymbol{\alpha}_{F(1-4)}$ are the Bézier polynomial coefficients of the ground reaction force, $\boldsymbol{q}, \dot{\boldsymbol{q}} \in \mathbb{R}^{2 \times N}$ are joint angles and joint velocities at the grid points, $vec(\cdot)$ is the vectorization operator for matrices. Equality constraints were imposed to satisfy forward kinematics:

$$\boldsymbol{rot}(q_k^1) \begin{bmatrix} l \\ 0 \end{bmatrix} + \boldsymbol{rot}(q_k^1 + q_k^2) \begin{bmatrix} l \\ 0 \end{bmatrix} + \begin{bmatrix} 0 \\ z_k \end{bmatrix} = 0 \tag{6}$$

$$\boldsymbol{J}(\boldsymbol{q}_k)\dot{\boldsymbol{q}}_k + \begin{bmatrix} 0 \\ \dot{z}_k \end{bmatrix} = \begin{bmatrix} 0 \\ 0 \end{bmatrix} \quad (k = 1, 2, \cdots, N) \tag{7}$$

where $\boldsymbol{rot} \in SO(2)$ is the rotation matrix; z_k and $\dot{z}_k$ are the height and velocity of the base at each grid point; $\boldsymbol{q}_k = [q_k^1, q_k^2]^T, \dot{\boldsymbol{q}}_k \in \mathbb{R}^{2 \times 1}$ are the kth column of $\boldsymbol{q}, \dot{\boldsymbol{q}}$.
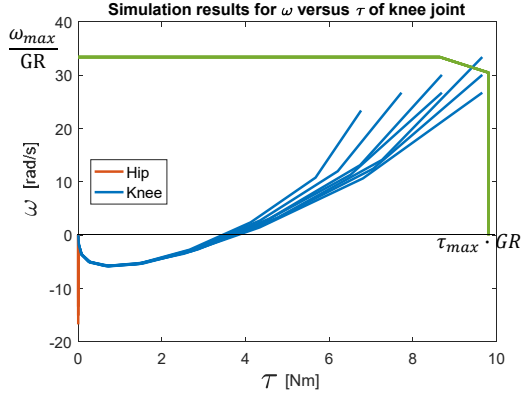
Fig. 3. The Admissible Operating Region (AOR) formed by the maximal speed and torque points from knee extensor model simulation. A typical motor's speed-torque curve scaled by gear ratio of 23:1 is plotted in green curve. Hip motor acts as a passive joint throughout the jumping up phase.

Since the thigh and shank links are assumed to be massless, joint torque $\boldsymbol{\tau}_k \in \mathbb{R}^{2 \times 1}$ could be reconstructed using $\boldsymbol{\tau}_k = \boldsymbol{J}(\boldsymbol{q}_k)^T \boldsymbol{F}_{GRF,k}$, where $\boldsymbol{J}(\boldsymbol{q}_k) \in \mathbb{R}^{2 \times 2}$ is the manipulator Jacobian of the foot relative to the hip.

The constraints on joint angle, angular velocity and torque could be formulated as

$$
\begin{aligned}
\boldsymbol{q}_{lb} &\leq \boldsymbol{q}_k \leq \boldsymbol{q}_{ub} \\
\dot{\boldsymbol{q}}_{lb} &\leq \dot{\boldsymbol{q}}_k \leq \dot{\boldsymbol{q}}_{ub} \quad (k = 1, 2, \cdots, N) \\
\boldsymbol{\tau}_{lb} &\leq \boldsymbol{\tau}_k \leq \boldsymbol{\tau}_{ub}
\end{aligned}
\tag{8}
$$

where vectors with subscripts lb and ub stand for constant vectors of lower bound and upper bound, respectively.

The jumping performance was evaluated by the maximal reachable height, $h_{max} := h_{to} + \frac{v_{to}^2}{2g}$, where h_{to} and v_{to} are the base height and speed at the moment of take-off.

The nonlinear optimization problem was formulated as

$$
\begin{aligned}
\min \quad & -h_{max} \\
s.t. \quad & \text{equality constraints: (6) and (7)} \\
& \text{inequality constraints: (8)}
\end{aligned}
\tag{9}
$$

MATLAB's $fmincon$ function was used to search for local optimal solutions. The parameters for the knee extensor model was chosen as follows: mass $m = 0.66$ kg, link length $l = 0.12$ m. Nine simulation runs were executed with maximal motor speed and torque constraints varied over a range where the maximal jumping height exceeds 0.5 m ($\tau : 6.9 - 9.8$ Nm; $\omega : 23.8 - 33.4$ rad/s). Simulations results are shown in Fig. 3.

C. Admissble Operating Region

Multiple simulation results from Section II-B are plotted in the speed-torque plane as shown in Fig. 3 in blue line. An actuator's $\omega - \tau$ curve scaled by gear ratio could be plotted on the same plane, shown as green line in Fig. 3. The part of blue lines enclosed by the actuator's $\omega - \tau$ curve is defined as Admissible Operating Region (AOR), which represents the set of motion admissible to the motor/gearbox pair. AOR is determined by the desired motion and the motor/gearbox

pair. AOR was used in the early stage of design to provide an intuitive and quantifiable tool to narrow down the range of the gear ratio and the set of actuators to choose from.

III. MECHANICAL AND CONTROL DESIGN

Dynamic maneuvers such as jumping require a robot to produce large force at high angular speed. Torque density $K_{ps} = \frac{\tau_{peak}}{m}$ [4] is the primary metric for actuator selection because it reflects an actuator's capability to create large ground reaction forces. However, as the scale of a robot decreases, the lack of motor speed becomes a limiting factor since higher angular velocity is needed to produce the same end-effector speed. Therefore, the balanced consideration between the requirements of motor torque and speed is mainly addressed in this section.

A. Actuator Selection

Thermal specific torque $K_{ts} = \frac{K_t}{m} \sqrt{\frac{1}{R_{th} R}}$ [18] was proposed as the metric for the direct drive robot Minitaur, which does not suffer from lack of speed because it forgoes gearboxes entirely. In contrast, MIT Cheetah [13] has relatively larger linkage length, hence motor speed is not the bottleneck for creating dynamic motions.

Our strategy is to strike a balance between torque and speed requirements by giving the same emphasis on motor's speed capability as on torque capability. Nonlinear optimization was used to validate the actuator choice in a more detailed model. As shown in Fig. 3, actuators reach their maximal torque and speed output simultaneously in the jumping scenario, which implies that maximal output power is also reached at the same time. In this case, maximal specific power $\frac{\tau_{max}}{m} \cdot \omega_{max}$ becomes an important parameter in indicating the ability of a motor to deliver power in jumping applications, because it takes into account both motors' torque and speed capabilities. These are a motor's intrinsic properties that are independent of gear ratio.

In order to compare motor performance under different metrics, the specific torque data of motors from Parker, Allied Motion, and Maxon are plotted in Fig. 4 against gap radius. The gap radius is chosen to make comparisons between motors because it is an important sizing parameter for torque density, which is defined as the "distance from the rotating axis to the center of the gap between permanent magnets and the stator" [4]. The maximal specific power data are plotted against gap radius in Fig. 5. While specific torque is close between motors with similar gap radius, Parker motors have the highest maximal specific power value under the same gap radius. Taking into account the dimensional limit of motor installation on a small-sized targeting robot platform (OD<50 mm; stack length<50 mm), Parker motor K044050 was chosen with gear ratio 23:1 from the analysis conducted in Section II-C.

B. Impact Force Mitigation

The impact force at the touch down instance is crucial in Quasi-Direct-Drive actuators because a large ground impulse may break gear teeth. The impact force is investigated by
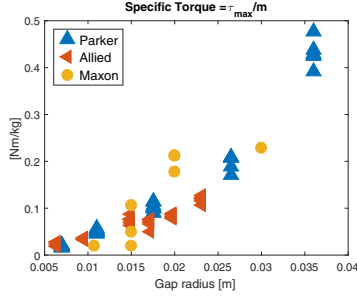
Fig. 4. Specific torque versus gap radius for a selection of commercial motors: Parker, Allied Motion, Maxon [19]
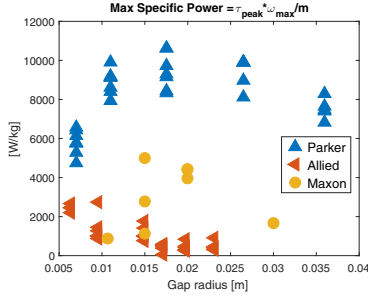

Fig. 6. Configuration of motors and the linkage design (left). Cross-section view of the HIP-KNEE module, showing the gearbox and motor (right)

Fig. 5. Maximal specific power versus gap radius for a selection of commercial motors

Fig. 7. Planetary gearbox design with three compound planet gears (left); curved upper-link design (middle); hip and knee motor module (right)

taking gearbox inertia into the impact model, which could be formulated as follows [20]:

$$\boldsymbol{D} \cdot (\dot{\boldsymbol{q}}^+ - \dot{\boldsymbol{q}}^-) = \boldsymbol{J}^T(\boldsymbol{q}_{impact}) \cdot \boldsymbol{F} + \boldsymbol{J}_x^T(\boldsymbol{q}_{impact}) \cdot F_x$$

$$\boldsymbol{D} = \begin{bmatrix} m & 0 & 0 & 0 \\ 0 & m & 0 & 0 \\ 0 & 0 & I_1 \cdot \gamma^2 & 0 \\ 0 & 0 & 0 & I_2 \cdot \gamma^2 \end{bmatrix} \quad (10)$$

where I_1 and I_2 are rotor inertias for joint 1 and 2; γ is the gear ratio; $\boldsymbol{q}, \dot{\boldsymbol{q}} \in \mathbb{R}^{4 \times N}$ are joint angle and velocity matrices; $\boldsymbol{q}_k := [x_k, z_k, q_k^1, q_k^2]^T$ is the kth column of $\boldsymbol{q}$; $\boldsymbol{q}_{impact}$ is the leg's joint angles at impact; $\dot{\boldsymbol{q}}^-, \dot{\boldsymbol{q}}^+ \in \mathbb{R}^{4 \times 1}$ are the velocity right before and after the impact; $\boldsymbol{F} \in \mathbb{R}^{2 \times 1}$ is the impact force from ground to the toe; $F_x \in \mathbb{R}$ is the impact force from the linear rail to the leg base; $\boldsymbol{J} \in \mathbb{R}^{2 \times 4}$ is the Jacobian of the toe; $\boldsymbol{J}_x \in \mathbb{R}^{1 \times 4}$ is the Jacobian of the base's horizontal position. The nominal inertias are constant since the link inertia is negligible ($< 15\%$) compared to gearbox inertia. The constraint $\boldsymbol{J} \cdot \dot{\boldsymbol{q}}^+ = \boldsymbol{0}$ makes sure that the foot does not slip with respect to the ground; the constraint $\boldsymbol{J}_x \cdot \dot{\boldsymbol{q}}^+ = 0$ makes sure the base does not break away from the linear rail. By solving the equations simultaneously, $\dot{\boldsymbol{q}}^+, \boldsymbol{F}$, and F_x could be expressed as

$$\begin{bmatrix} \dot{\boldsymbol{q}}^+ \\ \boldsymbol{F} \\ F_x \end{bmatrix} = \begin{bmatrix} \boldsymbol{D} & -\boldsymbol{J}^T & -\boldsymbol{J}_x^T \\ \boldsymbol{J} & 0 & 0 \\ \boldsymbol{J}_x & 0 & 0 \end{bmatrix}^{-1} \begin{bmatrix} \boldsymbol{D} \cdot \dot{\boldsymbol{q}}^- \\ 0 \\ 0 \end{bmatrix} \quad (11)$$

C. Foot Horizontal Offset

The knee extensor model from Section II-A assumes the foot and base are vertically aligned so that only the knee motor is requir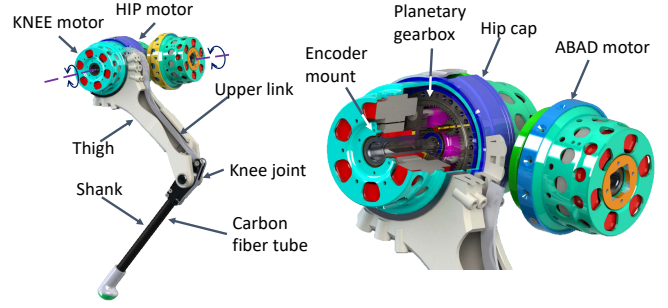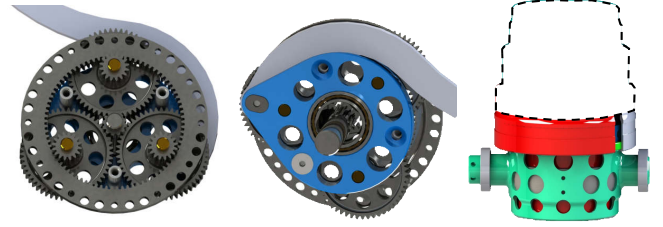ed in GRF production. In the detailed leg model, horizontal offset Δ_x is added to the list of optimization variables so that both hip and knee motors would contribute to GRF production. The gear ratio γ is also added to the list of optimization variables. The updated list of optimization variables $\boldsymbol{x}'_{opt}$ is defined as

$$\left[z_0, \gamma, \boldsymbol{\alpha}_{F(1-4)}^T, T_{st}, \Delta_x, vec(\boldsymbol{q})^T, vec(\dot{\boldsymbol{q}})^T, \boldsymbol{q}_{impact}^T \right]^T \quad (12)$$

The updated nonlinear optimization problem is posed as

$$\min \quad -\frac{h_{max}}{||\boldsymbol{F}||}$$

$$s.t. \quad \text{inequality constraints: (8)}$$

$$\text{equality constraints: (11)}$$

$$\begin{bmatrix} x_k \\ z_k \end{bmatrix} + \boldsymbol{rot}(q_k^1) \begin{bmatrix} l \\ 0 \end{bmatrix} + \boldsymbol{rot}(q_k^1 + q_k^2) \begin{bmatrix} l \\ 0 \end{bmatrix} = 0$$

$$\boldsymbol{J}(\boldsymbol{q}_k)\dot{\boldsymbol{q}}_k = 0$$

$$(13)$$

where impact force $\boldsymbol{F}$ could be calculated from (11). The objective function was chosen to be $-\frac{h_{max}}{||\boldsymbol{F}||}$ because it is desirable to have large maximal reachable height and smaller impact force. Optimization results from Section II-B serve as an initial guess in the more detailed model. Local optima could be found for the following parameters: Bézier polynomial coefficients $\boldsymbol{\alpha}_{F(1-4)} = [0, 7.8, 8.0, 21.1, 74.4, 0]^T$, $\gamma = 22.9$ and $h_{max} = 0.82 \ m$.

D. Optimization for Horizontal Jumping

Similar nonlinear optimization can be implemented to obtain optimized horizontal jumping. To do that, additional Bézier coefficients $\boldsymbol{\alpha}_{F_x}$ were added to parameterize the horizontal ground reaction force, as well as the horizontal
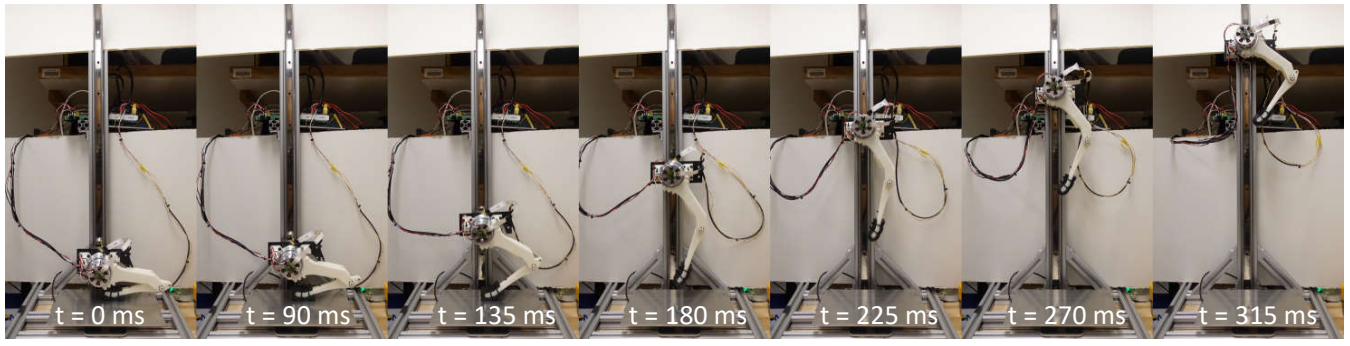
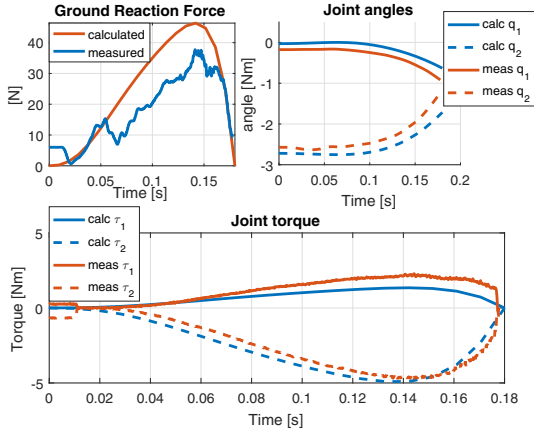Fig. 8. Sequential screenshots of one vertical jumping experiment

Fig. 9. Experiment data (blue) plotted against calculated values (red) for one vertical jump; ground reaction force (upper-left), joint angles (upper right), joint torques (bottom)

position and velocity. The cost is adjusted to take into account horizontal jumping distance instead of vertical height.

E. Hardware Integration

Having decided all the design parameters, a prototype leg was integrated as shown in Fig. 6. Each leg module is composed of three brushless DC (BLDC) motor modules. HIP, KNEE, and ABAD stand for hip joint, knee joint and abduction/adduction joints, respectively. The HIP and KNEE motor modules are placed coaxially and the hip joint has a 360 degree range of motion as shown in Fig. 6.

The planetary gearbox shown in Fig. 7 utilizes two-stage compound planet gears to provide the desired gear ratio while keeping the design compact. Taking the gear ratio from Section III-C, a large number of teeth combinations were enumerated and the optimal gear teeth choice emerged (γ = 23.36; sun gear: 12; planet gear: 16/53; ring gear: 81). The teeth number of sun gear and ring gear could both be divided by 3, but the phase difference between the two stages of a planet gear could not be maintained in the manufacturing process. To solve this problem, the planet gear teeth combination was chosen to be 16/53, which only shares the common factor of 1. This choice provides tunable backlash with a $2.1°$ increment in the gearbox assembly, very

similar to the working principle of a mechanical caliper.

The leg module shown in Fig. 2 (c) consists of a two-motor module (HIP and KNEE), the thigh and shank links, and the foot cushioned by sorbothane because of its shock-absorbing capability. The total mass of the leg is 0.64 kg while the weight of thigh and shank sums up to 0.06 kg, which is less than 10% of the total mass. Hence it could be neglected in the simulation model.

The electronic system of the robot leg consists of the following components: two Elmo Gold Twitter amplifiers were used for motor commutation, two RLS-RMB20 magnetic encoders were used to measure motor angle, ATI Mini40 F/T sensor was used to measure the ground reaction force created by the leg. The control loop runs at 4kHz on an Intel i5 desktop in Simulink Real-Time.

IV. RESULTS

A. Vertical Jumping

The leg module was mounted on a vertical linear rail, the force sensor installed beneath the jumping platform was used to measure ground reaction force. The Bézier polynomial coefficients for ground reaction force obtained by nonlinear optimization described in section II-B was applied. The leg was tethered to an off-board power supply and computer. The sequential snapshots of a single jump is shown in Fig. 8. The leg started from a crouched position, extended its leg rapidly and took off after 0.18 s, at the height of 0.2 m with take-off velocity 2.87 m/s. It reached a maximal height of 0.62 m.

Fig. 9 shows the calculated and measured parameters in one jump. Joint angles were recorded by joint encoders and joint torques were calculated as the production of current and motor torque constant k_t. As Fig. 9 shows on the upper-left figure, the measured ground reaction force matched the calculated value closely except for the time interval from $t = 0.06$ s to $t = 0.17$ s. The reason could be that at that time interval, high angular velocity induced large viscous friction, which was not considered in our dynamic model. The small peak at the early stage of stance phase might be caused by the elastic deformation of the sorbothane foot, which is intended to absorb ground impact upon touch-down. The lack of ground reaction force caused the base to accelerate slower than expected, so joint angles were deviated from calculated
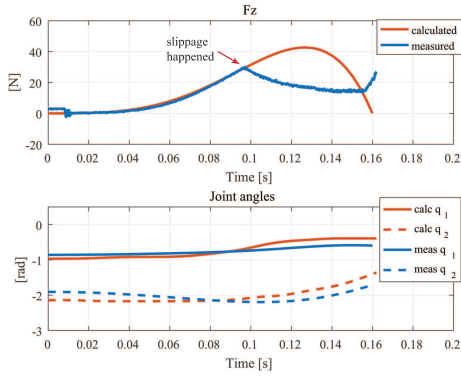
Fig. 10.   Vertical ground reaction force (top) and joint angles (bottom) for calculated and measured values in horizontal jump experiment

values, which resulted in the difference of leg configuration. This difference in manipulator Jacobian caused the measured joint torque to be off from calculated values.

B. Horizontal Jumping

In the horizontal jump experiment, the robot leg was rigidly attached to a 1.2 m boom made of a carbon fiber tube to restrict its motion in the lateral direction. All amplifiers were installed on the boom while the leg was tethered to off-board power sources. The total mass of the leg is 0.98 kg including the boom and electronics. The experiment was conducted to make the robot leg jump from a static crouched position, and then its motors produced torque to create a ground reaction force which made the robot leg leap forward. The horizontal force was added in a jumping forward model parametrized by a 5th order Bézier polynomial.

The vertical force and joint angle data is presented in Fig. 10. The ground reaction force followed calculated values closely in the early phase of stance, then it suddenly decreases. From the video, it has been observed that the foot slipped relative to ground which caused the leg to lose contact. It could be deduced that at around 0.095 s, friction was not sufficient to provide the desired horizontal ground reaction force, thus, the foot detached from the ground. Consequently, the joint angle deviated from calculated values drastically after 0.095 s. In spite of that, a maximal horizontal jumping distance of 0.72 m was observed. In future work, a more realistic model that includes the friction cone constraint will be used to eliminate slippage.

A video featuring the vertical and horizontal jumping experiment is available in the attachment.

V. Conclusion

In this paper, the design method of a robotic leg prototype for small-scale dynamic robots was presented. Inspired by the Quasi-Direct-Drive (proprioceptive actuator) design idea, the proposed method balances among requirements of impact mitigation, torque density and motor speed for a given task, and gives a systematic way of choosing design parameters including gear ratio. With the motor and gear ratio chosen from the analysis of nonlinear optimization, the robot leg

module could achieve a maximal jumping height of 0.62 m in vertical jump experiments. Horizontal jump experiments showed that the robot could achieve a maximal jumping distance of 0.72 m. Our future plan is to assemble a quadrupedal robot platform with this leg design to achieve highly dynamic motion.

References

[1] R. Alexander, "Exploring biomechanics. animals in motion," *Scientific American Library, New York*, vol. 247, 1992.

[2] K. Schmidt-Nielsen, *Scaling: why is animal size so important?* Cambridge University Press, 1984.

[3] M. N. Scholz, M. F. Bobbert, and A. K. van Soest, "Scaling and jumping: Gravity loses grip on small jumpers," *Journal of Theoretical Biology*, vol. 240, no. 4, pp. 554–561, 2006.

[4] S. Seok, A. Wang, D. Otten, and S. Kim, "Actuator design for high force proprioceptive control in fast legged locomotion," *IEEE International Conference on Intelligent Robots and Systems*, pp. 1970–1975, 2012.

[5] R. M. Walter and D. R. Carrier, "Ground forces applied by galloping dogs," *Journal of Experimental Biology*, vol. 210, no. 2, pp. 208–216, 2007.

[6] M. F. Bobbert, M. R. Yeadon, and B. M. Nigg, "Mechanical analysis of the landing phase in heel-toe running," *Journal of Biomechanics*, vol. 25, no. 3, pp. 223–234, 1992.

[7] Y. Sakagami, R. Watanabe, C. Aoyama, S. Matsunaga, N. Higaki, and K. Fujimura, "The intelligent ASIMO: system overview and integration," *IEEE/RSJ International Conference on Intelligent Robots and System*, vol. 3, no. October, pp. 2478–2483, 2002.

[8] D. W. Robinson, J. E. Pratt, D. J. Paluska, and G. A. Pratt, "Series elastic actuator development for a biomimetic walking robot," in *Advanced Intelligent Mechatronics, 1999. Proceedings. 1999 IEEE/ASME International Conference on*. IEEE, 1999, pp. 561–568.

[9] H. Asada and K. Youcef-Toumi, *Direct-drive Robots: Theory and Practice*. Cambridge, MA, USA: MIT Press, 1987.

[10] C. Carignan and K. Cleary, "Closed-loop force control for haptic simulation of virtual environments," *Haptics-e*, vol. 1, no. 2, pp. 1–14, 2000.

[11] S. Kalouche, "Design for 3d agility and virtual compliance using proprioceptive force control in dynamic legged robots," Master's thesis, CARNEGIE MELLON UNIVERSITY, 2016.

[12] H.-W. Park, P. M. Wensing, and S. Kim, "Online Planning for Autonomous Running Jumps Over Obstacles in High-Speed Quadrupeds," *Robotics: Science and Systems*, pp. 1–9, 2015.

[13] H.-W. Park, P. M. Wensing, and K. Sangbae, "High-speed bounding with the MIT Cheetah 2 : Control design and experiments," *The International Journal of Robotics Research*, vol. 36(2), pp. 167–192, 2017.

[14] National Geographic, "Super squirrel," 2014, [Online] Available: National Geographic: Super Squirrel. [Accessed 10 July 2017].

[15] R. J. Full, D. E. Koditschek, and R. J. Full, "Templates and anchors: neuromechanical hypotheses of legged locomotion on land," *The Journal of Experimental Biology*, vol. 2, no. 12, pp. 3–125, 1999.

[16] Ç. Dişibüyük and H. Oruç, "A generalization of rational bernstein–bézier curves," *BIT Numerical Mathematics*, vol. 47, no. 2, pp. 313–323, 2007.

[17] E. H. Doha, A. H. Bhrawy, and M. A. Saker, "Integrals of Bernstein polynomials: An application for the solution of high even-order differential equations," *Applied Mathematics Letters*, vol. 24, no. 4, pp. 559–565, 2011.

[18] G. Kenneally, A. De, and D. Koditschek, "Design Principles for a Family of Direct-Drive Legged Robots," *IEEE Robotics and Automation Letters*, vol. 1, no. 2, pp. 900–907, 2016.

[19] Maxon Motor, "Maxon motor catalog," [Online] Available: www.maxonmotorusa.com/.

[20] C. Glocker, "On frictionless impact models in rigid-body systems," *Philosophical Transactions of the Royal Society A: Mathematical, Physical and Engineering Sciences*, vol. 359, pp. 2385–2404, 2001.